PNAS RESEARCH ARTICLE | NEUROSCIENCE

KCTD1 regulation of Adenylyl cyclase type 5 adjusts striatal cAMP signaling

Yini Liao[a] and Brian S. Muntean[a,1]

Edited by Susan Amara, NIH, Bethesda, MD; received April 2, 2024; accepted September 19, 2024

Dopamine transfers information to striatal neurons, and disrupted neurotransmission leads to motor deficits observed in movement disorders. Striatal dopamine converges downstream to Adenylyl Cyclase Type 5 (AC5)-mediated synthesis of cAMP, indicating the essential role of signal transduction in motor physiology. However, the relationship between dopamine decoding and AC5 regulation is unknown. Here, we utilized an unbiased global protein stability screen to identify Potassium Channel Tetramerization Domain 1 (KCTD1) as a key regulator of AC5 level that is mechanistically tied to N-linked glycosylation. We then implemented a CRISPR/SaCas9 approach to eliminate KCTD1 in striatal neurons expressing a Förster resonance energy transfer (FRET)-based cAMP biosensor. 2-photon imaging of striatal neurons in intact circuits uncovered that dopaminergic signaling was substantially compromised in the absence of KCTD1. Finally, knockdown of KCTD1 in genetically defined dorsal striatal neurons significantly altered motor behavior in mice. These results reveal that KCTD1 acts as an essential modifier of dopaminergic signaling by stabilizing striatal AC5.

dopamine | cAMP | striatum | motor learning | KCTD1

Significance

Dopamine guides motor function in striatal neurons by activating receptors that modulate activity of Adenylyl Cyclase Type 5 (AC5). AC5 synthesizes the second messenger cAMP and polymorphisms in its encoding gene, *ADCY5*, are causal to movement disorders. Here, we report AC5 stability is influenced by N-linked glycosylation. We find that Potassium Channel Tetramerization Domain 1 (KCTD1) mediates interaction between AC5 and the deglycosylating enzyme N-glycanase 1 (NGLY1). KCTD1/NGLY1 actively maintain cellular abundance of AC5. Removal of KCTD1 leads to decreased AC5 as well as reduced dopaminergic signaling in striatal neurons. Selective knockdown of KCTD1 in striatal circuits subsequently impairs motor coordination in mice. Altogether, we demonstrate the importance of KCTD1 in striatal signaling and mouse behavior.

The striatum of the brain plays an essential role in animal movement (1). Prominent examples pertain to movement disorders, with the prototypic case inherent to Parkinson's disease where loss of dopaminergic inputs to the striatum drives pathology (2). Yet hyperkinetic movement disorders void of neurodegeneration are also associated with striatal and dopaminergic abnormalities (3). A number of therapies for movement disorders have centered on dopamine replacement (e.g., l-3,4-dihydroxyphenylalanine) (4, 5), largely due to the role of dopamine as a critical modulator of synaptic strength in striatal neurons (6). However, dopamine does not directly change membrane potential in striatal neurons (7, 8). Rather, stimulation of cognate dopamine G protein-coupled receptors (GPCRs) regulates the catalytic activity of AC enzymes, which synthesize the second messenger cyclic adenosine 3′,5′-monophosphate (cAMP) (9). Homeostasis of striatal cAMP is indispensable for proper motor function as evidenced by a portfolio of clinical variants in the striatal cAMP system that facilitate manifestation of hyperkinetic movement disorders. Genes include *TH* (10, 11), *SLC6A3* (12), *DRD2* (13), *GNAO1* (14), *GNAL* (15), *GNB1* (16), and *PDE10A* (17, 18). At the heart of cAMP in the striatum is Adenylyl Cyclase Type 5 (AC5), the isoform responsible for approximately 80% of striatal cAMP (19), where numerous mutations in the encoding gene *ADCY5* give rise to dyskinesia (20). Despite the importance of striatal cAMP signaling, there is a scarcity of studies focused on the interplay between AC5 regulation and dopamine signal decoding.

Decades of foundational research has detailed biochemical properties of AC5 (21, 22) as well as crystal (23, 24) and full-length cryo-electron microscopy (25) structures. Yet far less is known concerning the players that control the AC5 level within cells. It has been reported that AC5 can be ubiquitinated by the TRIP-Br1/XIAP complex, which leads to subsequent degradation (26). On the other hand, AC5 forms a macromolecular complex with Golf heteromeric proteins (Gαolf-Gβ2-Gγ7), which is also vital for maintaining stability (27). Elimination of the Gβ chaperone, PhLP1, significantly destabilized AC5 (27). Therefore, we were inspired to investigate whether additional proteins that interact with the ubiquitous G protein subunit, Gβ, would contribute toward AC5 stability.

Numerous members of the Potassium Channel Tetramerization Domain containing (KCTD) protein family have been found to interact with the Gβγ obligate dimer (28–31). The majority of KCTD are Cullin3 adapters that provide scaffolding for the ubiquitination of substrate proteins (32–36). Two members, KCTD2 and KCTD5, have been shown to facilitate ubiquitination of Gβ and consequently promote downregulation of Gβγ (28, 30). Because Gβγ has been implicated in AC5 stability (27), our goal was to determine whether the KCTD family at large may also influence AC5 abundance at the protein level.

Author affiliations: [a]Department of Pharmacology and Toxicology, Medical College of Georgia, Augusta University, Augusta, GA 30912

Author contributions: Y.L. and B.S.M. designed research; Y.L. and B.S.M. performed research; Y.L. and B.S.M. analyzed data; and B.S.M. wrote the paper.

The authors declare no competing interest.

This article is a PNAS Direct Submission.

[1]To whom correspondence may be addressed. Email: bmuntean@augusta.edu.

This article contains supporting information online at https://www.pnas.org/lookup/suppl/doi:10.1073/pnas.2406686121/-/DCSupplemental.

Published October 16, 2024.

We began with an unbiased screen that identified KCTD1 as a positive regulator of AC5. Cell-based experiments were then implemented to understand KCTD1's mechanism of action. We report that N-linked glycosylation of AC5 correlated with lower amounts of AC5. Removal of glycosylation by the enzyme N-glycanase 1 (NGLY1) promoted AC5 level. We observed that KCTD1 mediates an interaction between NGLY1 and AC5. Coexpression of KCTD1/NGLY1 reduced AC5 glycosylation and ubiquitination, which collectively increased AC5 abundance. Our data reveal that KCTD1 actively promotes AC5 stability. Knockdown of KCTD1 in striatal neurons significantly lowered AC5 level and reduced the magnitude of dopaminergic signaling downstream to cAMP. Loss of KCTD1 in genetically defined striatal neurons profoundly impacted rodent motor learning and coordination in a circuit-selective manner. Our study further amplifies the importance of AC5-cAMP regulators in striatal physiology and identifies KCTD1 as a critical modulator of dopamine signaling.

Results

KCTD1 Increases the Protein Level of AC5. We began with a modified version of previously described unbiased global protein stability screen (37) to interrogate whether members of the KCTD family may adjust the level of AC5. To achieve robust, high-throughput quantification of the protein level, we engineered a construct encoding the fusion of AC5-Venus-P2A-mRuby3 (Fig. 1*A*). Transient transfection of HEK293 cells enabled confocal imaging of AC5 (Venus) and a housekeeping protein (mRuby3) at 1:1 stoichiometry from a single plasmid (Fig. 1*B*). Therefore, we cotransfected HEK293 cells with our imaging plasmid along with each individual KCTD from a previously described library of KCTD-myc-Flag constructs that express at similar levels in HEK293 cells (29, 38). Cells were fixed after 48 h for confocal imaging to obtain fluorescence intensity ratio of Venus to mRuby3. We found that the AC5 level was significantly increased by overexpression of KCTD1 and KCTD15 (Fig. 1*C* and *SI Appendix*, Fig. S1*A* and Table S1). A phylogenetic tree of the KCTD family revealed that KCTD1/KCTD15 not only represent their own distinct subclade (*SI Appendix*, Fig. S1*B*) but also share 80% identity overall (*SI Appendix*, Fig. S1*C*). Analysis of single-cell RNA-sequencing data from striatal neurons revealed that KCTD1 is the most abundant KCTD in striatal MSNs, at least at the transcript level (39). On the other hand, KCTD15 exhibited almost zero expression in medium-spiny neurons (MSNs) (Fig. 1*D*). Due to the importance of striatal AC5 (19, 40), we focused our investigation on KCTD1 rather than KCTD15.

We next transiently transfected HEK293 cells with Flag-AC5 in the presence (KCTD1-mVenus) or absence (mVenus) of KCTD1. We then arrested translation by treating cells with cycloheximide and quantified the AC5 level by western blotting with an anti-Flag antibody (Fig. 1 *E* and *F*). First, we observed that AC5 level was significantly augmented in the presence of KCTD1 at the baseline (nontreated) time point (Fig. 1*G*). The rate of AC5 degradation was significantly reduced by exogenous KCTD1 expression (Fig. 1*H*) and therefore KCTD1 cells contained a higher amount of AC5 after 4 h of cycloheximide compared with control (Fig. 1*I*). Because AC5 has been reported to undergo ubiquitin-mediated degradation (26), we hypothesized that KCTD1 may play a role in promoting the AC5 level and consequently disrupt degradation. We reasoned that interference with AC5 ubiquitination would hinder cycloheximide-mediated degradation, which we tested by mutating C-terminal lysine residues reported to undergo ubiquitination (Flag-AC5-KA: K1242A, K1244A, K1246A). The AC5-KA mutant still exhibited a significantly higher baseline level in KCTD1 overexpression cells compared with control (*SI Appendix*, Fig. S1 *E–G*). Treating cells with cycloheximide further revealed that AC5-KA degradation in control cells was reduced to a similar rate (*SI Appendix*, Fig. S1*H*) and level (*SI Appendix*, Fig. S1*I*) as KCTD1 cells, suggesting that KCTD1 did not influence ubiquitin-mediated processes. To pinpoint how KCTD1 increased AC5 abundance, we next considered N-linked glycosylation, which has been reported to contribute toward regulation of several AC isoforms (41). We generated an N-terminal Flag epitope AC5 construct where asparagine residues predicted to undergo glycosylation were converted to glutamine (Flag-AC5-NQ: N873Q, N880Q, N890Q, N975Q). Indeed, AC5-WT exhibited two bands, whereas the AC5-NQ mutant appears as the lower nonglycosylated band (*SI Appendix*, Fig. S1*D*). We then performed the cycloheximide experiment in cells expressing AC5-NQ. We observed that KCTD1 did not exhibit significant effects on AC5-NQ (*SI Appendix*, Fig. S1 *J* and *K*). Specifically, KCTD1 was no longer able to influence the baseline AC5-NQ protein level (*SI Appendix*, Fig. S1*L*), degradation rate (*SI Appendix*, Fig. S1*M*), or amount of AC5 after 4 h of cycloheximide (*SI Appendix*, Fig. S1*N*). Given that AC5-NQ was also not completely degraded in our cycloheximide observation window, our data indicate that glycosylation plays a role in AC5 maintenance. Our results suggest that KCTD1 likely promotes AC5 stability through interplay with the glycosylation process. In summary, our findings identify KCTD1 as a regulator of the cellular AC5 level.

KCTD1 Forms a Complex with NGLY1 to Regulate AC5. In our working model, glycosylation destabilizes the AC5 level, whereas the nonglycosylated AC5 was observed to be more abundant. This raises the question of how AC5 glycosylation could be influenced by KCTD1. N-linked glycosylation occurs during protein synthesis in the ER through a process involving hundreds of enzymes (42). It therefore does not appear logical that mature KCTD1 would interfere with nascent AC5 glycosylation. In contrast to the multifaceted glycosylation process, there is a relative scarcity of mammalian "deglycosylating" enzymes (43). We investigated whether one such well-conserved enzyme, the cytosolic NGLY1 (peptide:N-glycanase) (44), could lead to removal of glycosylation on AC5 and subsequently aid stability. We first examined whether KCTD1 could interact with NGLY1 in HEK293 cells by transfecting KCTD1-Flag and hemagglutinin (HA)-NGLY1 followed by immunoprecipitation (IP) with an anti-Flag antibody (Fig. 2*A*). Indeed, we observed an interaction between the two proteins, which prompted us to assess complex formation with AC5. We performed IP with an anti-HA antibody in cells transfected with Flag-AC5, KCTD1-Venus, and HA-NGLY1 (Fig. 2*B*). In total lysate, AC5 was observed as the deglycosylated form (lower band) in the presence of NGLY1 or KCTD1 with NGLY1. We also found that NGLY1-KCTD1-AC5 were pulled down with the anti-HA antibody. However, AC5 was not detected in the IP sample with NGLY1 in the absence of KCTD1. Nonetheless, data indicate that KCTD1-NGLY1 prompt AC5 stability by removal of N-linked glycosylation.

We next wanted to examine whether NGLY1-KCTD1 would hinder ubiquitination of AC5. For this purpose, we developed a dual luminescence-based IP assay to quantify AC5 ubiquitination. We fused Nanoluciferase (Nluc) to the C terminus of Flag-AC5 (Flag-AC5-Nluc). We also attached Firefly luciferase (Fluc) at the N terminus of a ubiquitin containing the G76V mutation (Fluc-Ubiq). The G76V mutation on ubiquitin increases detection by enabling resistance to ubiquitin hydrolase cleavage (45).

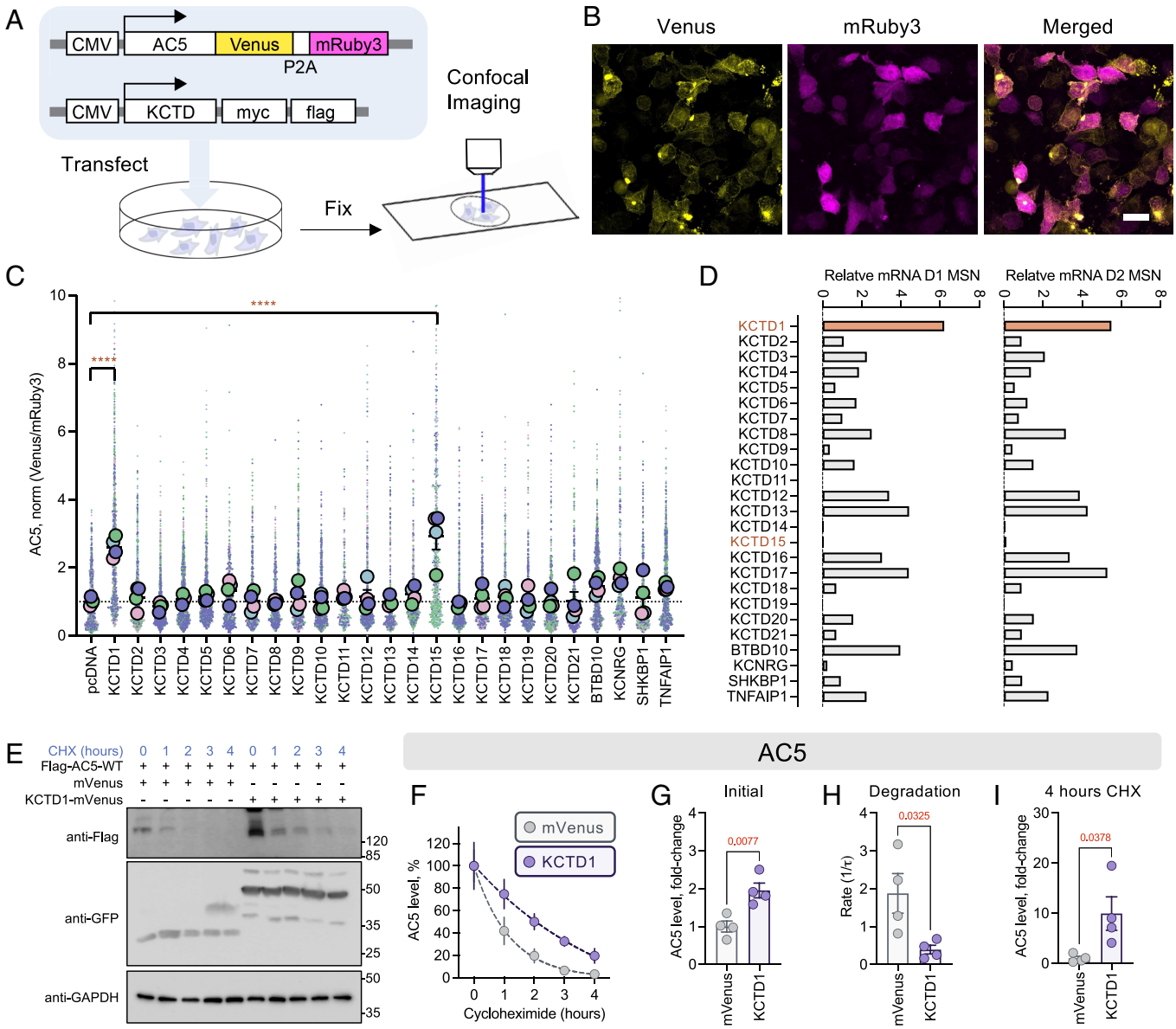

Fig. 1. KCTD1 increases the protein level of AC5. (*A*) Scheme of imaging pipeline to transfect cells with AC5-Venus-P2A-mRuby3 and each individual KCTD ORF for confocal imaging fixed cells. (*B*) Representative confocal images of AC5 (Venus) and a housekeeping protein (mRuby3). The white scale bar represents 20 μm. (*C*) Superplot of the AC5 protein level. Each small dot represents Venus:mRuby3 ratio for a single cell, normalized to pcDNA control. Each large circle represents the average for one biological replicate. Colors are coded such that matched dots and circles represent the same replicate. Error bars and statistical tests were performed on the biological replicates of each sample (n = 4). One-way ANOVA was performed with Dunnett's multiple comparisons test to pcDNA control. F = 8.965, R^2 = 0.7418 (****P < 0.0001). (*D*) Relative Kctd expression in mouse striatal D1- and D2-MSNs, data curated from ref. 39. (*E*) Representative western blot of Flag-AC5-WT cells treated with cycloheximide (20 μg/mL final concentration) prior to lysis. (*F*) Quantification of the Flag-AC5-WT level (anti-Flag antibody) relative to 0-h cycloheximide treatment. n = 4 biological replicates. (*G*) Quantification of the Flag-AC5-WT level (anti-Flag antibody) at 0-h cycloheximide treatment (i.e., no treatment). n = 4 biological replicates, unpaired *t* test, P = 0.0077. (*H*) Quantification of the Flag-AC5-WT degradation rate, 1/τ, at 0-h cycloheximide treatment (i.e., no treatment). n = 4 biological replicates, unpaired *t* test, P = 0.0325. (*I*) Quantification of the Flag-AC5-WT level (anti-Flag antibody) at 4-h cycloheximide treatment. n = 4 biological replicates, unpaired *t* test, P = 0.0378. Unless indicated, all data are represented as mean ± SE of the mean. Also, *SI Appendix*, Fig. S1.

Transfected cells were treated overnight with a proteasome inhibitor (MG132; 10 μM), AC5 IP was performed utilizing the Flag epitope, and ubiquitination of AC5 was quantified by luminescence readings on a plate reader (Fig. 2*C*). We first validated our approach by confirming specificity of the Fluc (D-Luciferin) and Nluc substrates (Nano-Glo) to produce robust luminescence only when paired with Fluc-Ubiq and Flag-AC5-Nluc lysates, respectively (*SI Appendix*, Fig. S2*A*). Moreover, our IP-luminescence protocol resulted in luminescence from Flag-AC5-Nluc samples, whereas signal was not detected in Flag-AC5-negative control (*SI Appendix*, Fig. S2*B*). The dual luminescence strategy was then utilized to examine ubiquitin in Flag-AC5-Nluc IP samples by calculating the ratio of Fluc (Ubiquitin) to Nluc (AC5). We observed that overexpression of KCTD1 provided an approximate threefold decrease in Ubiquitin detection on AC5 pulldown samples in our assay (Fig. 2*D*). Intriguingly, the presence of NGLY1 also had a comparable effect. Introducing both KCTD1 and NGLY1 almost completely abolished detection of Ubiquitin on AC5. Total lysates exhibited similar luminescence from both Nluc and Fluc, indicating that the IP ratio was not compromised by sample preparation (*SI Appendix*, Fig. S2 *C* and *D*). Similarly, raw Nluc (AC5) values from IP samples were relatively consistent (*SI Appendix*, Fig. S2*E*) as the assay was sensitive to detect lower Ubiquitin (Fluc) induced by KCTD1 and NGLY1 (*SI Appendix*, Fig. S2*F*). As an additional control, we repeated the experiments with Flag-AC5-KA-Nluc where putative lysine sites available for ubiquitination were

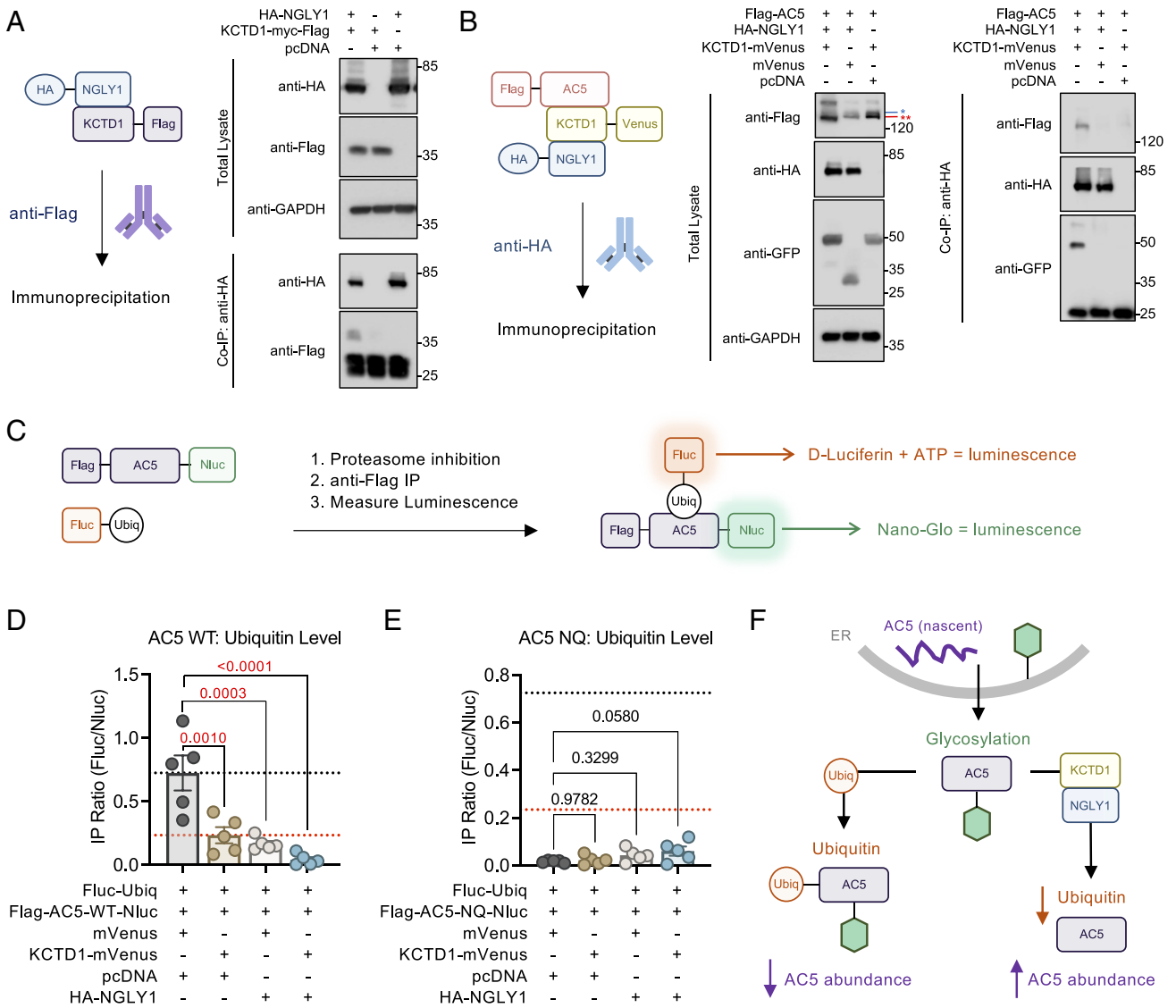

Fig. 2. KCTD1 forms a complex with NGLY1 to increase the AC5 protein level. (*A*) IP of HA-NGLY1 from HEK293 cells with the anti-HA antibody followed by probing for KCTD1-myc-Flag with an anti-Flag antibody. Representative blot from three independent experiments. (*B*) IP of HA-NGLY1 from HEK293 cells with the anti-HA antibody followed by probing for Flag-AC5 with an anti-Flag antibody and KCTD1-mVenus with an anti-GFP antibody. Representative blot from three independent experiments. (*C*) Scheme of dual luminescence assay to measure Ubiquitin associated with Flag-AC5 following anti-Flag pulldown. Proteasome inhibition was achieved by overnight treatment of cells with MG132 (10 μM). (*D*) Quantification of luminescence ratio (Fluc/Nluc) from anti-Flag IP from Flag-AC5-WT-Nluc lysates. n = 5 biological replicates, One-way ANOVA: F = 15.02, R^2 = 0.7379 (****P < 0.0001). The average ratio in the presence of KCTD1 (red dotted line) or the absence of KCTD1 (black dotted line) is indicated. (*E*) Quantification of luminescence ratio (Fluc/Nluc) from anti-Flag IP from Flag-AC5-NQ-Nluc lysates. n = 5 biological replicates, One-way ANOVA: F = 2.666, R^2 = 0.3333 (P = 0.0830). The average ratio from Flag-AC5-WT-Nluc in the presence of KCTD1 (red dotted line) or the absence of KCTD1 (black dotted line) is indicated. (*F*) Model based on our data that AC5 degradation is promoted by glycosylation, which is influenced by KCTD1. Unless indicated, all data are represented as mean ± SE of the mean. Also, *SI Appendix*, Fig. S2.

converted to alanine. As anticipated, the ubiquitin level in AC5-KA samples was very low and therefore KCTD1/NGLY1 imparted no impact on the assay (*SI Appendix*, Fig. S2*G*). Finally, we examined a glycosylation deficient version of AC5 (Flag-AC5-NQ-Nluc). Ubiquitination was not detected in either the presence or absence of KCTD1/NGLY1 (Fig. 2*E*). Overall, data suggest that glycosylation of AC5 is important for subsequent ubiquitination. Our findings support a model where KCTD1/NGLY1 reduces the level of Ubiquitin associated with AC5, which leads to increased AC5 abundance (Fig. 2*F*).

KCTD1 Is an Essential Regulator of Striatal cAMP Signaling. We next asked whether KCTD1-mediated regulation of AC5 protein level would have functional consequences and hence sought to investigate whether cAMP signaling would be impacted. First, HEK293 cells were transiently transfected with Flag-AC5 and a Förster resonance energy transfer (FRET)-based cAMP reporter (^{T}Epac^{VV}) (46) in the presence (KCTD1-myc-flag) or absence (pcDNA) of KCTD1 (*SI Appendix*, Fig. S3*A*). We then performed real-time FRET imaging in live cells during application of the diterpene AC activator forskolin. Cells expressing KCTD1 exhibited a significantly greater cAMP response than control (*SI Appendix*, Fig. S3*B*), which aligns with an increased level of AC5 protein. Since KCTD1 promotes AC5 signaling, we asked the corollary question: Would elimination of KCTD1 reduce cAMP mobilization? To examine in the relevant neuronal context, we cultured primary striatal neurons from the *cAMP E*ncoded *R*eporter (*CAMPER*) mouse line, which conditionally express the ^{T}Epac^{VV} biosensor (47). We then incorporated a CRISPR approach by using an adeno-associated virus (AAV) vector that conditionally encodes *Staphylococcus aureus* Cas9 (SaCas9) and a single guide RNA (sgRNA) (CMV-FLEX-SaCas9-U6-sgRNA) (48).

We inserted a *Kctd1* sgRNA sequence into the plasmid (scrambled sgRNA used as control), generated AAV particles in house (49), and infected primary striatal neurons. To simultaneously unlock *CAMPER* biosensor expression and enable the CRISPR/SaCas9 knockout, cultures were also infected with a single AAV encoding Cre and dTomato (hSyn-Cre-P2A-dTomato) (Fig. 3*A*).

Given similarity between KCTD1 and KCTD15, we first validated antibody specificity before confirming knockout efficiency. Western blotting with either anti-KCTD1 or anti-KCTD15 antibody was performed on lysates of transfected HEK293 cells (either KCTD1-Flag, KCTD15-Flag, KCTD8-Flag, or pcDNA), which confirmed selectivity of our anti-KCTD1 antibody (*SI Appendix*, Fig. S3*C*). Western blotting on lysates from primary striatal cultures demonstrated that *Kctd1* sgRNA completely eliminated detection of KCTD1, thus confirming our knockout approach (Fig. 3*B*). Loss of KCTD1 in primary cultures meanwhile coincided with a significant reduction in AC5 level. To examine the possibility of redundancy or compensation, we probed three other prominent striatal cyclases (AC1, AC3, and AC9) (39). However, we did not observe changes in the protein level of other ACs in Control versus *Kctd1* sgRNA (Fig. 3*B*). The loss of AC5 suggested that cAMP signaling could be compromised and that prompted FRET imaging of the ^{T}Epac^{VV} sensor in primary striatal neurons (Fig. 3*C*). Bath application of forskolin induced robust cAMP responses (Fig. 3*D*) that were significantly reduced in *Kctd1* sgRNA neurons compared to Control sgRNA (Fig. 3*E*).

We next wanted to investigate the potential role of KCTD1 to influence signaling in intact neuronal circuits from adult animals. *CAMPER* mice were stereotactically injected with a mixture of the same AAV particles at P0-P2 and acute brain slices were prepared at 6 to 10 wk of age for 2-photon confocal-FRET imaging of cAMP dynamics (Fig. 4*A*). For these experiments, we focused on the dorsal striatum where the AC5 level is particularly prominent (50). Similar to primary cultures, bath application of forskolin increased neuronal cAMP in brain slices where *Kctd1* sgRNA responses were significantly reduced compared with control (*SI Appendix*, Fig. S4 *A* and *B*). The striatum forms two distinct circuits of MSNs with the prototypic hallmark pertaining to a segregated expression of dopamine receptor subtypes: i) one population enriched in D1R that couples to stimulatory Gαolf to increase AC5-mediated cAMP production (D1-MSN), ii) one population enriched in D2R that couples to Gαi for inhibition of AC5-mediated cAMP production (D2-MSN) (51, 52). The critical physiological role of dopamine inspired assessment of KCTD1's influence on signaling through endogenous dopamine receptors. Bath application of a selective D1R partial agonist (SKF38393) induced a stimulatory cAMP response that was significantly greater in Control compared with *Kctd1* sgRNA (*SI Appendix*, Fig. S4*C*). Bath application of a D2R selective agonist (quinpirole) produced robust inhibitory cAMP responses that were also significantly reduced in *Kctd1* sgRNA compared with Control (*SI Appendix*, Fig. S4*D*). The data demonstrate that signaling through endogenous dopamine receptors was compromised by loss of KCTD1 in both striatal circuits.

We next investigated how decoding of endogenous synaptic dopamine events may be impacted by loss of KCTD1. To address this question, we inserted a stimulating electrode into brain slices to electrically evoke dopamine release while simultaneously recording cAMP responses. To benchmark the approach, we first utilized brain slices from *Drd1a*^{Cre}*:CAMPER* mice to isolate D1R signaling. A single 10

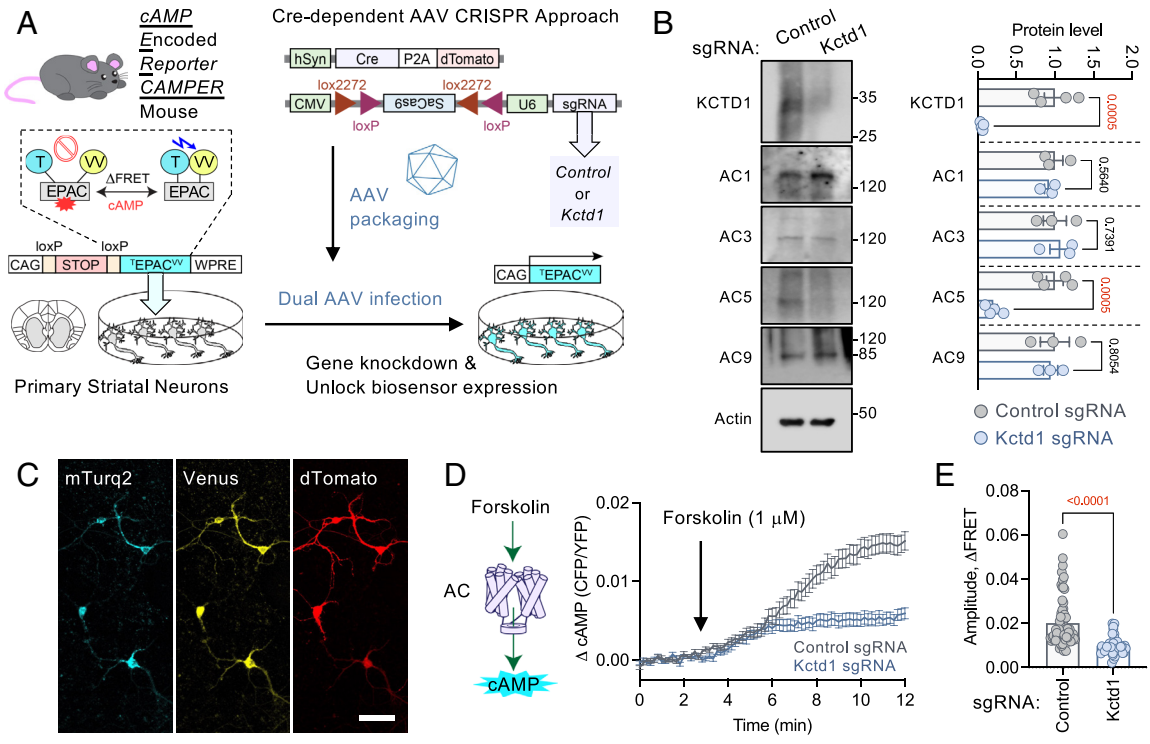

Fig. 3. KCTD1 regulates the striatal AC5 level and forskolin-induced cAMP signaling. (*A*) Schematic of approach for CRISPR/SaCas9-mediated knockdown of *Kctd1* in *CAMPER* expressing primary striatal neurons. (*B*) Western blot quantification from primary striatal neurons (Control or *Kctd1* knockdown) for KCTD1 (n = 4), AC1 (n = 3), AC3 (n = 3), AC5 (n = 4), and AC9 (n = 3). Unpaired *t* test, $P = 0.0005$ (KCTD1), $P = 0.5654$ (AC1), $P = 0.7391$ (AC3), $P = 0.0005$ (AC5), and $P = 0.8054$ (AC9). (*C*) Representative images of primary striatal *CAMPER* neurons expressing the ^{T}Epac^{VV} biosensor and AAV-Cre-P2A-dTomato. The white scale bar represents 50 μm. (*D*) Average traces of real-time cAMP response to bath application of 1 μM forskolin in Control sgRNA (n = 68 neurons) and *Kctd1* sgRNA (n = 45 neurons) primary striatal *CAMPER* neurons. (*E*) Quantification of maximum cAMP response amplitude of primary striatal *CAMPER* neurons to 1 μM forskolin. n = 68 neurons Control sgRNA, n = 45 neurons *Kctd1* sgRNA, unpaired nonparametric *t* test, Mann–Whitney test ($U = 361$), $P < 0.0001$. All data are represented as mean ± SE of the mean. Also, *SI Appendix*, Fig. S3.

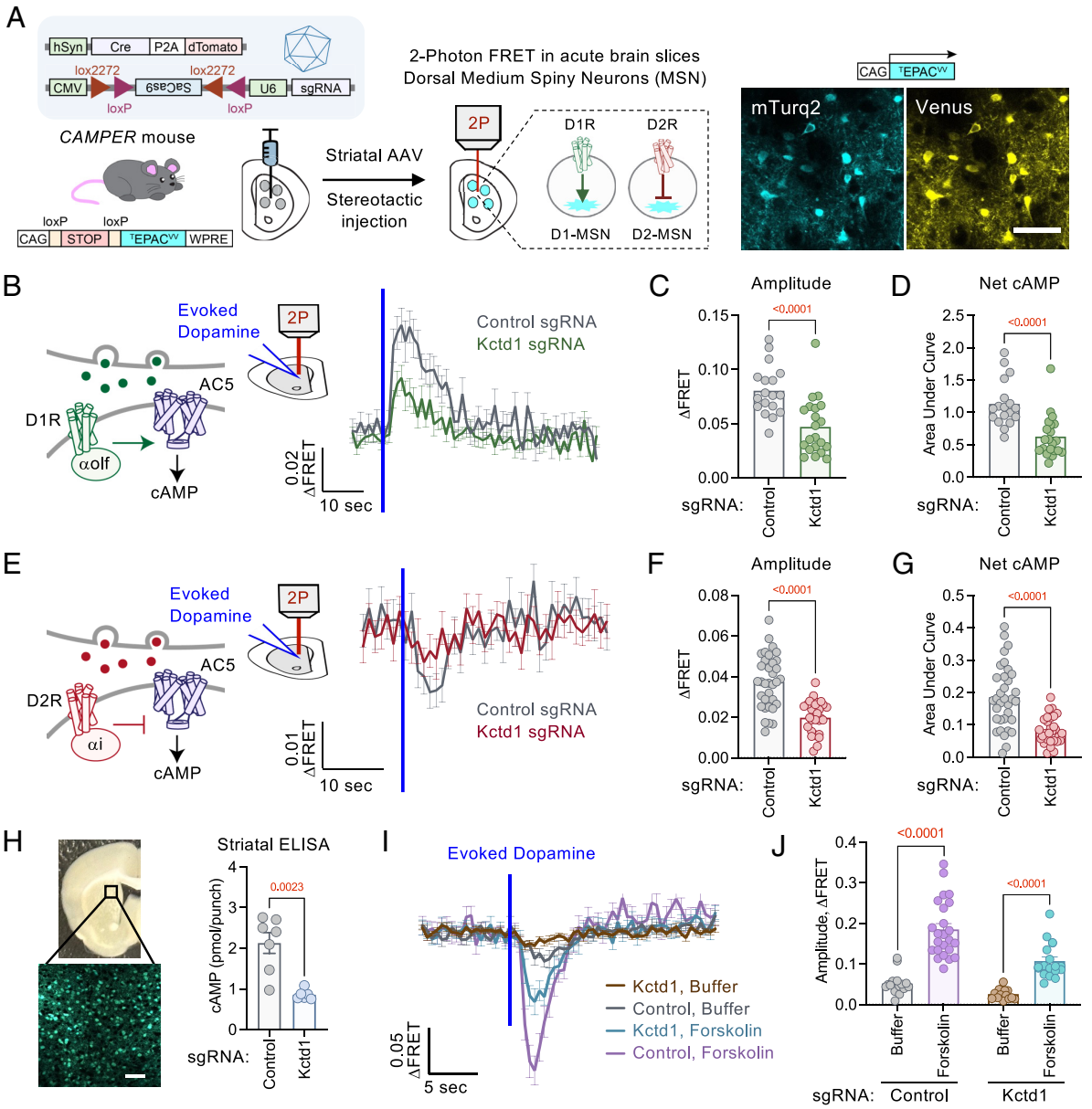

Fig. 4. KCTD1 is an essential regulator of striatal dopamine cAMP signaling. (*A*) Schematic of approach for CRISPR/SaCas9-mediated knockdown of *Kctd1* for 2-photon FRET imaging in acute brain slices from *CAMPER* mice. Representative images of $^{T}Epac^{VV}$ fluorescence in 300 μm acute brain slice during live imaging. White scale bar represents 50 μm. (*B*) Average traces of electrically evoked D1R cAMP in Control sgRNA (n = 18 neurons/six animals) and *Kctd1* sgRNA (n = 21 neurons/seven animals) acute brain slices from *CAMPER* mice. (*C*) Quantification of maximum D1R cAMP response amplitude in acute brain slices from *CAMPER* mice following electrical stimulation. n = 18 neurons Control sgRNA (six animals), n = 21 neurons *Kctd1* sgRNA (seven animals), unpaired nonparametric *t* test, Mann–Whitney test ($U = 56$), $P < 0.0001$. (*D*) Quantification of net D1R cAMP response, as calculated by area under the response curve, in acute brain slices from *CAMPER* mice following electrical stimulation. n = 18 neurons Control sgRNA (six animals), n = 21 neurons *Kctd1* sgRNA (seven animals), unpaired nonparametric *t* test, Mann–Whitney test ($U = 40$), $P < 0.0001$. (*E*) Average traces of electrically evoked D2R cAMP in Control sgRNA (n = 34 neurons/six animals) and *Kctd1* sgRNA (n = 29 neurons/seven animals) acute brain slices from *CAMPER* mice. (*F*) Quantification of maximum D2R cAMP response amplitude in acute brain slices from *CAMPER* mice following electrical stimulation. n = 34 neurons Control sgRNA (six animals), n = 29 neurons *Kctd1* sgRNA (seven animals), unpaired nonparametric *t* test, Mann–Whitney test ($U = 135$), $P < 0.0001$. (*G*) Quantification of net D2R cAMP response, as calculated by area under the response curve, in acute brain slices from *CAMPER* mice following electrical stimulation. n = 34 neurons Control sgRNA (six animals), n = 29 neurons *Kctd1* sgRNA (seven animals), unpaired nonparametric *t* test, Mann–Whitney test ($U = 167.5$), $P < 0.0001$. (*H*) ELISA-based quantification of cAMP from dorsal striatal tissue punches in 300 μm slices from Control sgRNA (n = 7 animals) and *Kctd1* sgRNA (n = 6 animals) *CAMPER* mice. Unpaired nonparametric *t* test, Mann–Whitney test ($U = 1$), $P = 0.0023$. (*I*) Average traces of electrically evoked D2R cAMP in either buffer or 1 μM forskolin: Control sgRNA (buffer n = 15 neurons/seven animals, forskolin n = 24 neurons/seven animals), *Kctd1* sgRNA (buffer n = 14 neurons/eight animals, forskolin n = 18 neurons/eight animals). (*J*) Quantification of maximum D2R cAMP response amplitude in acute brain slices from *CAMPER* mice following electrical stimulation. Control sgRNA (buffer n = 15 neurons/seven animals, forskolin n = 24 neurons/seven animals) unpaired nonparametric *t* test, Mann–Whitney test ($U = 4$), $P < 0.0001$. *Kctd1* sgRNA (buffer n = 14 neurons/eight animals, forskolin n = 18 neurons/eight animals) unpaired nonparametric *t* test, Mann–Whitney test ($U = 1$), $P < 0.0001$. All data are represented as mean ± SE of the mean. Also, *SI Appendix*, Fig. S4.

ms pulse generated a robust stimulatory cAMP response that was completely blocked by inclusion of a selective D1R antagonist (SCH23390), indicating that the electrical response was specific to dopamine (*SI Appendix*, Fig. S4*E*). To probe evoked dopamine responses at the D2R, we utilized *Drd2*^{Cre}*:CAMPER* mice. Here, electrical stimulation produced an inhibitory cAMP response that was blocked by the selective D2R antagonist sulpiride (*SI Appendix*, Fig. S4*F*). We next evoked dopaminergic-cAMP responses in brain slices from AAV-Cre/CRISPR injected *CAMPER* mice and classified responses offline based on directionality of the cAMP response (D1-MSN: stimulatory, D2-MSN: inhibitory). D1-MSNs produced a robust stimulatory cAMP response (Fig. 4*B*) where the signal in

Kctd1 sgRNA was significantly reduced compared with Control sgRNA (Fig. 4 *C* and *D*). Similarly, D2-MSNs generated an inhibitory cAMP response following electrical stimulation (Fig. 4*E*) and *Kctd1* sgRNA was also significantly reduced compared with Control (Fig. 4 *F* and *G*). These results led to the hypothesis that the lower AC5 level in *Kctd1* sgRNA would reduce the baseline cAMP level. Consequently, there would not be as much cAMP available for degradation following inhibitory signaling (i.e., D2R→Gαi), and thus, such responses would be compromised. To test this hypothesis, we first measured the total cAMP level in *CAMPER* slices from dorsal striatal tissue punches utilizing an Enzyme-Linked Immunosorbent Assay (ELISA) kit. We observed approximately 50% reduction in baseline cAMP in *Kctd1* sgRNA samples compared with Control (Fig. 4*H*). To determine whether striatal D2R responses are indeed dependent on basal cAMP, we acutely bath applied low-dose forskolin (1 μM for 5 min) to *CAMPER* slices and then evoked endogenous dopamine release while recording 2P-cAMP responses (Fig. 4*I*). In Control sgRNA animals, enhancing the cAMP baseline with forskolin resulted in a significant (~3.5 fold) increase in inhibitory D2R signaling compared with normal recording buffer (Fig. 4*J* and *SI Appendix*, Fig. S4*G*). Similarly in *Kctd1* sgRNA slices, inclusion of forskolin significantly enhanced evoked D2R inhibitory responses relative to normal buffer (Fig. 4 *I* and *J* and *SI Appendix*, Fig. S4*H*). Altogether our data demonstrate that KCTD1 plays a major role in regulating striatal cAMP signaling that likely emanates at the level of AC5 to influence decoding of endogenous neurotransmission.

Loss of KCTD1 Induces Striatal Circuit-Specific Effects on Motor Coordination and Learning. The basal ganglia shapes motor behavior in part through integration of activity between D1- and D2-MSNs (Fig. 5*A*) (51, 53). The striatal role of *Kctd1* in motor behavior has not been investigated. To study cell-type specific effects, we stereotactically injected AAV particles encoding CMV-FLEX-SaCas9-U6-sgRNA (Ctrl: control sequence, or Kctd1: targeting *Kctd1*) into the dorsal striatum of established striatal Cre-driver lines at P0-P2 (Fig. 5*B*). The *Drd1a*^{Cre} line was used to generate D1-MSN control (D1 Ctrl sgRNA) and D1-MSN *Kctd1* knockdown (D1 Kctd1 sgRNA) cohorts. *Adora2a*^{Cre} enabled D2-MSN control (D2 Ctrl sgRNA) and D2-MSN *Kctd1* knockdown (D2 Kctd1 sgRNA). When mice reached 2 mo of age, a series of behavioral tests that engage striatal circuitry was performed (Fig. 5*C*). Our behavioral schedule enabled assessment of coordination (backward walking), dystonic pathology (hindlimb clasping), and motor learning (accelerating rotarod) (54, 55). After motor learning, our timeline allowed for retrieval of motor memory by repeating the rotarod challenge 7 and 14 d after initial training. Motor coordination and clasping were reexamined after rotarod motor learning as well. The analysis began with motor coordination by assessment of ability to coordinate paws while walking backward on a rotarod. Three trials were conducted at P56 and then again at P77. At both initial and final time points, D1 Kctd1 sgRNA performed significantly worse during the backward walking assessment compared with D1 Ctrl sgRNA (Fig. 5*D* and *SI Appendix*, Fig. S5*A*). On the other hand, there were no statistical differences in reverse walking between D2 Kctd1 sgRNA and D2 Ctrl sgRNA (Fig. 5*D* and *SI Appendix*, Fig. S5*A*). The next measurement was the action pattern of hindlimbs in tail-suspended mice, which represents a rodent manifestation of hyperkinetic movement disorders observed in patients. D1 Kctd1 sgRNA exhibited a significant clasping score compared with D1 Ctrl sgRNA, whereas in the D2 cohort, both control and *Kctd1* sgRNA animals displayed normal outward extension of the hindlimbs (Fig. 5*E* and *SI Appendix*, Fig. S5*B*). We next examined motor learning by performing three intraday trials over five consecutive days on an accelerating rotarod (56). The three intraday trials were then repeated 7 (Day 12) and 14 (Day 19) d after the initial motor learning paradigm. D1 Ctrl sgRNA steadily improved rotarod performance, mastered the task by Day 4, and repeated success on Days 12 and 19 (Fig. 5*F* and *SI Appendix*, Fig. S5 *C* and *D*). D1 Kctd1 sgRNA performed significantly worse than D1 Ctrl sgRNA on the first day (Fig. 5 *F* and *G* and *SI Appendix*, Fig. S5*C*). Strikingly, D1 Kctd1 sgRNA failed to improve on the rotarod over time and exhibited a significantly reduced learning rate compared with D1 Ctrl (Fig. 5*G*). On Day 1 in the D2-MSN cohort, D2 Kctd1 sgRNA displayed a significantly lower latency to fall from the rotarod compared with D2 Ctrl sgRNA (Fig. 5 *H* and *I* and *SI Appendix*, Fig. S5*E*). Both groups of mice learned the task and showed daily improvements until mastery was achieved. Yet by Day 2 the D2 Kctd1 sgRNA rapidly learned the task and were outperforming D2 Ctrl sgRNA group by Day 3. Indeed, the learning rate of D2 Kctd1 sgRNA was significantly greater than D2 Ctrl sgRNA (Fig. 5*I*). Upon challenging motor memory retrieval both 7 and 14 d later, both sets of D2-MSN mice maintained their performance with no statistical differences (*SI Appendix*, Fig. S5*F*). Overall, behavior assessment strongly suggests that striatal knockdown of KCTD1 in D2-MSN selectively modulates motor learning relative to other motor abilities. Yet in D1-MSN, KCTD1 was essential for both motor coordination and motor learning.

Discussion

This study provides evidence that KCTD1 is a major regulator of AC5 glycosylation, ubiquitination, and protein level. This allows KCTD1 to play an essential role in shaping dopaminergic signal decoding downstream to cAMP in both D1- and D2-MSNs. Loss of KCTD1 in dorsal striatal MSNs results in circuit-specific impairments in motor learning and coordination. Our data add KCTD1 to a growing list of striatal cAMP regulators that modulate motor function. The illustrative model in *SI Appendix*, Fig. S5*G* provides a framework for how KCTD1-mediated regulation of AC5 contributes to the basal ganglia circuitry required for motor skills.

The critical role of cAMP signaling in nearly every cell type of the body has prompted considerable efforts toward understanding AC structures (23–25, 57, 58) and enzymatic properties (21, 22). AC5 in particular is hallmarked by regulatory components that shape sensitization of enzymatic activity (59–61). Yet comparatively little has been reported on AC5 stability. One mechanism governing AC5 stability stems from macromolecular complex formation with stimulatory heterotrimeric G proteins (Gαolf, Gβ, and Gγ) where striatal elimination of the Gβ chaperone PhLP1 significantly reduces the level of AC5 (27). This mode of AC5 regulation supports a model where the cell maintains homeostasis between G proteins and effectors. Appropriate stoichiometry is consistent with the idea of preassembled signaling complexes on the membrane (62). While many KCTD proteins interact with Gβγ in an agonist-induced manner, we previously reported that KCTD1 is a notable exception (29). This suggests that KCTD1 would be unlikely to directly regulate the Gβ level or offset the AC5 level by disturbing G protein abundance. On the other hand turnover of AC5 is facilitated through ubiquitin-mediated degradation by the TRIP-Br1/XIAP complex (26). Our findings add to this model in that KCTD1 protects AC5 from ubiquitin-dependent degradation. This mechanism is supported by demonstration that KCTD1, unlike many other KCTD, is not a Cullin 3 substrate adapter (35). Interaction between AC5 and KCTD1 would be unproductive in regard to ubiquitination. We further evolve the ubiquitin-turnover model of AC5 by building off of

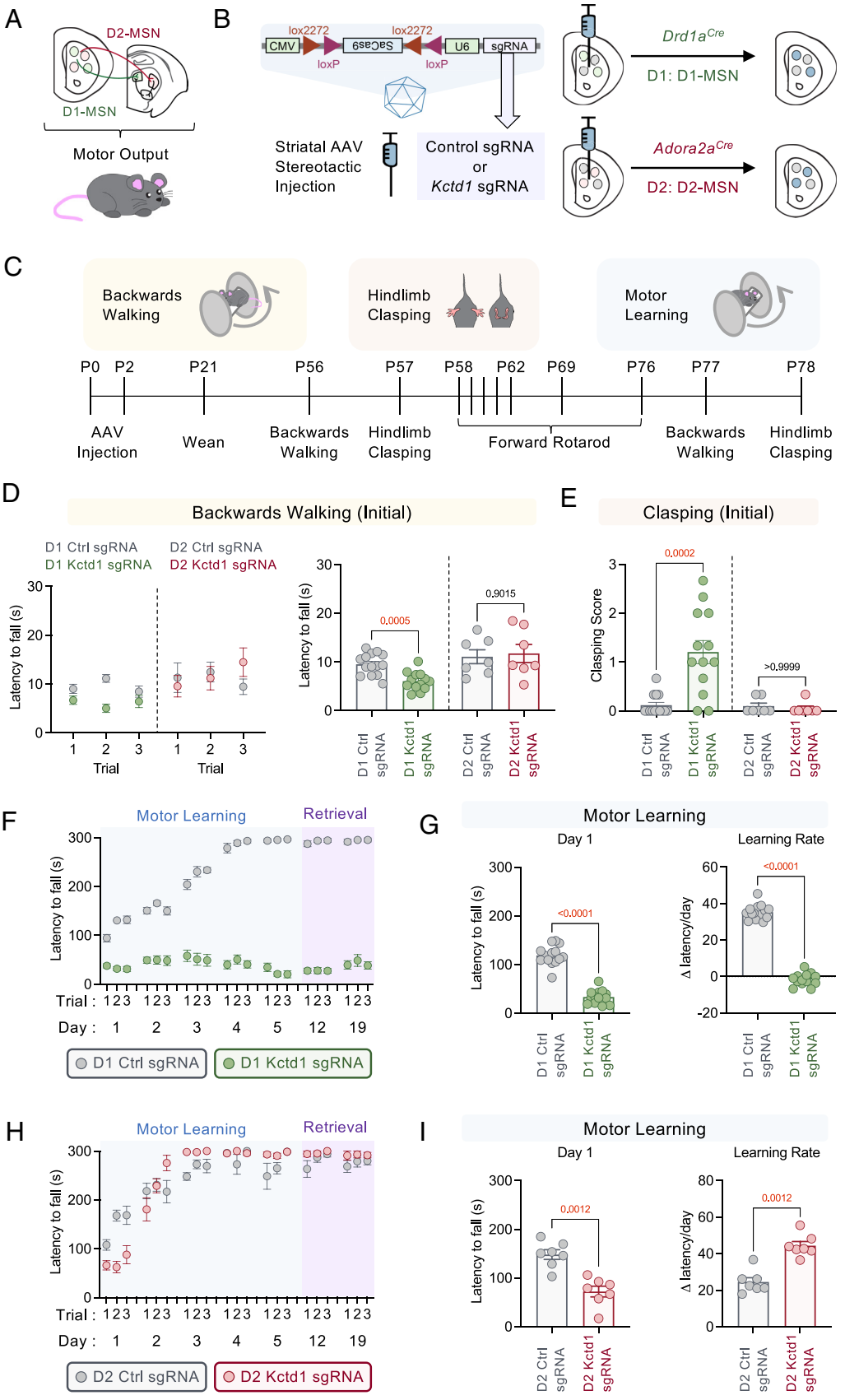

Fig. 5. Loss of KCTD1 imparts striatal circuit-specific effects on motor properties. (*A*) Schematic of basal ganglia circuit in motor control. (*B*) Schematic of approach to knockdown *Kctd1* in dorsal striatal D1- and D2-MSNs via AAV injection of Cre-dependent CRISPR/SaCas9 in *Drd1a*^{Cre} and *Adora2A*^{Cre} mice, respectively. (*C*) Timeline of mouse behavior experiments. (*D*) Quantification of initial backward walking before motor learning. *Drd1a*^{Cre} (D1 Ctrl sgRNA, n = 14: seven male, seven female; D1 Kctd1 sgRNA, n = 13: eight male, five female) unpaired nonparametric *t* test, Mann–Whitney test ($U = 23$), $P = 0.0005$. *Adora2A*^{Cre} (D2 Ctrl sgRNA, n = 7: three male, four female; D2 Kctd1 sgRNA, n = 7: three male, four female) unpaired nonparametric *t* test, Mann–Whitney test ($U = 23$), $P = 0.9015$. (*E*) Quantification of initial hindlimb clasping scores before motor learning. *Drd1a*^{Cre} (D1 Ctrl sgRNA, n = 14: seven male, seven female; D1 Kctd1 sgRNA, n = 13: eight male, five female) unpaired nonparametric *t* test, Mann–Whitney test ($U = 21$), $P = 0.0002$. *Adora2A*^{Cre} (D2 Ctrl sgRNA, n = 7: three male, four female; D2 Kctd1 sgRNA, n = 7: three male, four female) unpaired nonparametric *t* test, Mann–Whitney test ($U = 21$), $P > 0.9999$. (*F*) Quantification of latency to fall trials on accelerating rotarod for D1 Ctrl sgRNA (n = 14: seven male, seven female) and D1 Kctd1 sgRNA (n = 13: eight male, five female) mice. (*G*, *Left*) Quantification of average latency to fall on the first day (Day 1) for D1 Ctrl sgRNA (n = 14: seven male, seven female) and D1 Kctd1 sgRNA (n = 13: eight male, five female). Unpaired nonparametric *t* test, Mann–Whitney test ($U = 0$), $P < 0.0001$. (*Right*) Quantification of the learning rate in D1 Ctrl sgRNA (n = 14: seven male, seven female) and D1 Kctd1 sgRNA (n = 13: eight male, five female). Unpaired nonparametric *t* test, Mann–Whitney test ($U = 0$), $P < 0.0001$. (*H*) Quantification of latency to fall trials on accelerating rotarod for D2 Ctrl sgRNA (n = 7: three male, four female) and D2 Kctd1 sgRNA (n = 7: three male, four female) mice. (*I*, *Left*) Quantification of average latency to fall on the first day (Day 1) for D2 Ctrl sgRNA (n = 7: three male, four female) and D2 Kctd1 sgRNA (n = 7: three male, four female) mice. Unpaired nonparametric *t* test, Mann–Whitney test ($U = 1$), $P = 0.0012$. (*Right*) Quantification of the learning rate in D2 Ctrl sgRNA (n = 7: three male, four female) and D2 Kctd1 sgRNA (n = 7: three male, four female) mice. Unpaired nonparametric *t* test, Mann–Whitney test ($U = 1$), $P = 0.0012$. All data are represented as mean ± SE of the mean. Also, *SI Appendix*, Fig. S5.

the previous observation that ACs are subject to N-linked glycosylation (41), a posttranslational modification that can influence protein stability (63). Our findings demonstrate that the AC5 protein level is increased by preventing glycosylation (e.g., mutation of N-linked glycosylation residues). The presence of KCTD1 increased the half-life of wild-type AC5; however, the glycosylation-deficient AC5 mutant was no longer regulated by KCTD1. Rather our mechanistic studies revealed that KCTD1 interacts with both AC5 and the N-glycanase (deglycosylating enzyme) NGLY1. Without KCTD1 overexpression, we were

unable to detect interaction between AC5 and NGLY1, suggesting that KCTD1 mediates an association between the proteins. This is entirely consistent with established roles of most KCTD proteins, which serve to endow macromolecular complex formation through a combination of shared Broad-complex, Tramtrack, and Bric-à-brac/poxvirus and zinc finger domains and unique C termini (64). Experiments further demonstrated that overexpression of KCTD1 or both KCTD1/NGLY1 was sufficient to reduce AC5 glycosylation and ubiquitination. We take this as evidence that by adjusting the glycosylation state of AC5, KCTD1 appears to prevent ubiquitination and promote the AC5 level.

In alignment with our model that KCTD1 actively promotes the AC5 level, knockout of KCTD1 in striatal neurons significantly reduced the AC5 level and cAMP signaling. Our data further uncover that AC5 downregulation is not met with functional compensation of other mammalian ACs. Due to the effect on AC5 level, loss of KCTD1 elicited a profound impact on decoding synaptically released dopamine. In D1-MSNs, evoked dopamine led to a significantly reduced stimulatory cAMP response in the absence of KCTD1. As D1R couples to Gαs/olf for direct AC5 activation, adjustments to the cyclase level critically modify the extent of signaling (65). These data functionally validate our observation at the protein level that other striatal ACs are not up-regulated in absence of KCTD1 and provide support for AC5 being responsible for the majority of striatal cAMP synthesis (19). Yet in D2-MSNs without KCTD1, dopaminergic signaling was also compromised. As D2R activate Gαi to exert an inhibitory effect on AC5 catalytic activity (21, 22), we believe that the explanation for dampened dopamine responses in D2-MSNs is more nuanced. D2-MSNs have been reported to have higher basal cAMP and increased excitability relative to D1-MSNs (55, 66). This allows dopamine, through D2R inhibition of cAMP, to play a major role in long-term depression (6). Our data show that knockdown of KCTD1 lowers baseline cAMP in striatal brain slices, prompting us to propose that these D2-MSNs would have less cAMP available for clearance following AC5 inhibition from D2R activation. When the cAMP baseline was elevated by application of forskolin, evoked D2R inhibitory cAMP responses were significantly enhanced in both control and KCTD1 knockdown. This supports the notion that basal cAMP may be a major determinant of striatal D2R inhibitory cAMP signaling. While not explored in this study, we believe that this helps explain transcriptional differences between D1- and D2-MSNs. Relatively higher levels of basal cAMP in D2-MSNs could be attributed to their selective expression of the Gαolf-coupled receptors A2AR and GPR6 (39). A2AR is activated by multiple sources of adenosine (67, 68) and GPR6 exhibits constitutive activity (69, 70). Overall, our data reflect previous work demonstrating that mice lacking AC5 exhibit significant impairments in striatal D1R and D2R signaling (71).

Dopamine is thought to stimulate the direct pathway of the basal ganglia (D1-MSN) and inhibit the indirect pathway (D2-MSN), where either scenario results in prokinetic motor effects (1, 9). Because motor processes are facilitated by the coordinated action between D1- and D2-MSNs, it is not surprising that global loss of AC5 results in motor dysfunction (71, 72). Loss of KCTD1 in either striatal circuit led to motor pathology with a greater severity of phenotypes in D1-MSN knockdown compared with D2-MSN knockdown. Based on our signaling data, we believe that this is the case because D1-MSNs were unable to be activated by dopamine and relay concomitant motor signals to the Globus pallidus/Substantia nigra. D1-MSNs have been reported to take a leading role in motor learning, particular during early stages (73). Loss of KCTD1 in dorsal D1-MSNs completely blunted motor learning and resulted in impaired coordination during backward walking. Strikingly, we also observed hindlimb clasping in D1-MSN knockdown, which reflects a dystonic phenotype. D1-MSN-driven pathology is consistent with the clinical strategy of targeting the M4 muscarinic receptor (Gαi/o coupled), which is enriched in D1-MSNs, to provide efficacy in some cases of dystonia (74). These receptors are thought to minimally, if at all, contribute to signaling in D2-MSNs (39, 75). Loss of KCTD1 in D2-MSNs did not result in dystonic clasping or coordination deficits. These animals displayed initial motor learning deficits that significantly improved, resulting in an overall increased learning rate. We propose that decreased D2-MSN activity limits initial performance which then enables D1-MSN in the direct pathway to strongly promote early-phase motor learning (73). In regard to other regulators of the AC5 level, striatal knockout of PhLP1 blunted motor learning (27) while global XIAP knockout mice do not exhibit irregular motor learning on the rotarod (76). Thus, we add KCTD1 to an emerging list of KCTDs associated with motor dysfunction in either human patients (KCTD17) (77) or mouse models (KCTD5) (78).

Our findings predict that KCTD1 would contribute toward motor pathology in patients. In contrast, *KCTD1* human polymorphisms have been associated with dental anomalies (79) and cutis aplasia of the scalp (80). Structural studies have pointed toward protein misfunction of encoded *KCTD1* variants (81, 82); however, their effect on AC5 remains unknown. Curiously, we report that KCTD1 is a critical mediator of NGLY1 and the rare autosomal recessive disorder Congenital disorder of deglycosylation (CDDG) arises from an *NGLY1* deficiency. The clinical spectrum of CDDG pathology includes numerous neurological phenotypes and most patients display patterns of hyperkinetic movement disorders (83). A recent study of twelve individuals reported that every CDDG patient exhibited motor pathology (84). Deeper connections between NGLY1 and the cAMP cascade have been limited by the embryonic lethality observed in *Ngly1*$^{-/-}$ mice (85). The correlation between NGLY1/KCTD1 interaction and the role of NGLY1 in motor pathology may be of intrigue in future work.

A few additional limitations to our study are worth emphasizing. First, the design of our screen does not take into consideration the KCTD expression level, impact of KCTD knockout, or activity-dependent regulation of protein stability. Second, given the developmental nature of CDDG, profiling behavior from KCTD1 knockdown in adult mice would provide a more comprehensive understanding toward the role of cAMP signaling in the striatum. In D2-MSN knockdown of KCTD1, probing the role of endogenous stimulatory GPCRs and the role of Gβγ sensitization of AC5 would add mechanistic insight toward baseline cAMP influence on D2R signaling.

Overall, our study provides important insight into the rules and outcomes of AC5 stability. We further broaden the physiological importance of striatal cAMP regulation in the context of movement control. Our work highlights a role for KCTD1 in neuronal signaling, thus adding to the functional landscape of the KCTD family.

Materials and Methods

Experimental Model and Subject Details. Every experimental procedure utilizing mice was approved by Augusta University's Institutional Animal Care and Use Committee in compliance with guidelines set forth by the NIH. Mice were maintained under standard housing conditions with a 12 h light/dark cycle with continuous access to food and water. The following strains were utilized: i) *CAMPER* [C57BL/6-Gt(ROSA)26Sortm1(CAG-ECFP*/Rapgef3/Venus*)Kama/J] (RRID:IMSR_JAX:032205), ii) *Drd1a*^{Cre} [B6.FVB(Cg)-Tg(Drd1-cre)EY262Gsat/Mmucd] (RRID:MMRRC_030989-UCD), iii) *Drd2*^{Cre} [STOCK Tg(Drd2-cre)ER43Gsat/

Mmucd] (RRID:MMRRC_017268-UCD), and iv) *Adora2a*^{Cre} [B6.FVB(Cg)-Tg(Adora2a-cre)KG139Gsat/Mmucd] (RRID:MMRRC_036158-UCD). Genotypes were verified from DNA samples utilizing established PCR protocols for each line. Mice were further bred to obtain *Drd1a*^{Cre}*-CAMPER* and *Drd2*^{Cre}*-CAMPER* strains, as described (47). No statistical methods were used to determine sample sizes. Experiments involved both male and female mice.

Method Details.

Bioinformatics. UniProt was utilized to align human KCTD protein sequences. Phylogeny was visualized using Phylo.io rendering. Direct comparison between KCTD1 (Q719H9) and KCTD15 (Q96SI1) sequences was performed in UniProt. Supplemental data published by Gokce et al. were curated for comparison of relative KCTD mRNA in mouse striatal D1- and D2-MSNs (39).

Molecular biology. The following plasmids were obtained from Addgene: mVenus-N1 (#27793), pcDNA3.1 (#128034), pAAV-hSyn-Cre-P2A-dTomato (#107738), pAAV-FLEX-SaCas9-U6-sgRNA (#124844), pAAV2/5 (#104964), pAdDeltaF6 (#112867). The ^{T}Epac^{VV} biosensor has previously been described (46). A previously generated library of KCTD mammalian expression clones containing a C-terminal myc-Flag was utilized (29). KCTD1-mVenus was generated by insertion of synthesized DNA encoding mVenus (Twist Biosciences) at the C-terminal NotI/EcoRV sites on KCTD1-myc-flag. The AC5-Venus-P2A-mRuby3 plasmid was generated by inserting a custom synthesized DNA fragment (Twist Biosciences) containing the Venus-P2A-mRuby3 into AgeI and BamHI sites of the previously described Flag-AC5 expression construct (86). Venus-P2A-mRuby3 was subsequently replaced with a codon-optimized Nluc (Twist Bioscience) via KpnI and BamHI sites to generate Flag-AC5-Nluc. Flag-AC5-KA was generated by inserting a synthesized DNA fragment (Twist Biosciences) containing lysine to alanine mutations (K1242A, K1244A, K1246A) into the AgeI and BamHI sites of Flag-AC5. Flag-AC5-KA-Nluc was generated by cloning the synthesized insert with lysine to alanine mutations into Flag-AC5-Nluc via AgeI and KpnI sites. Flag-AC5-NQ was generated by inserting a synthesized DNA fragment (Twist Biosciences) containing asparagine to glutamine mutations (N873Q, N880Q, N890Q, N975Q) into the Bsu36I and AgeI sites of Flag-AC5. Flag-AC5-NQ-Nluc was generated by cloning the synthesized insert with asparagine to glutamine mutations into Flag-AC5-Nluc via Bsu36I and AgeI sites. N-terminal HA epitope was fused to human NGLY1 in pTwist mammalian expression vector at NotI and NheI sites. Fluc-Ubiq was generated by N-terminal fusion of Fluc to a chain of three GSG separated ubiquitin (human sequence with G76V mutation) at NotI and NheI sites in pTwist. pAAV-FLEX-SaCas9-U6-sgRNA with a *Kctd1* targeting sequence was generated by ligation of FLEX-SaCas9-U6 and a synthesized *Kctd1* sgRNA insert (Twist Biosciences) into the pAAV backbone of pAAV-hSyn-Cre-P2A-dTomato via triple ligation at XbaI, KpnI, and PmlI sites. The Control sgRNA sequence (5′-CGGAGACCACGGCAGGTCTCA-3′) has been previously described (48). The *Kctd1* targeting sequence (5′-ACGTCGATGTGGACGGGTGCG-3′) for SaCas9 was designed using CRISPOR 5.01 (87). All plasmids generated in this paper were confirmed by whole plasmid sequencing (Plasmidsaurus).

Cell culture. Human embryonic kidney cells (Lenti-X HEK293T; Takara Bio #632180) were cultured in Dulbecco's Modified Eagle Medium (Gibco #11995) supplemented with 7.5% Fetalgro EX (RMBio; FGX-BBT), MEM nonessential amino acids, 100 units/mL of penicillin, and 100 μg/mL of streptomycin. Cells were grown at 37 °C in a humidified incubator with constant 5% CO_2. Transient plasmid transfection was performed as previously described with polyethylenimine (Polysciences #23966-100) and OptiMEM (Gibco #11058021) on PDL (Gibco #A38904) coated dishes or glass coverslips (38).

Adeno-associated virus production. A previously described protocol was utilized to generate AAV particles encoding pAAV-hSyn-Cre-P2A-dTomato, pAAV-FLEX-SaCas9-U6-Control sgRNA, and pAAV-FLEX-SaCas9-U6-*Kctd1* sgRNA (49). Briefly, HEK293 cells were triple transfected with packaging plasmids (pAAV2/5 and pAdDeltaF6) along with our pAAV of interest followed by the viral chloroform extraction protocol (49). Concentrated viral titers were approximated to 10^{13} GC/mL via PCR before freezing in aliquots at −80 °C.

Western blotting. Transfected HEK293 cells and primary striatal neuron cultures were harvested 24 h after transfection and 7 d after plating, respectively. As indicated in the text, cells were treated with cycloheximide (Thermo Fisher Scientific #J66901-03) at a final concentration of 20 μg/mL. Cells were resuspended in ice-cold lysis buffer containing Phosphate-Buffered Saline (PBS) supplemented with 150 mM NaCl, 1% Triton-X, and protease inhibitor (Thermo Fisher Scientific #A32955) followed by sonication for 15 s at 30% power (FisherBrand #FB50110). Protein concentration was determined by using the Pierce 660 nm reagent (Thermo Fisher Scientific #22660) and samples were diluted to identical concentrations. Total lysates were then incubated with an sodium dodecyl sulfate (SDS)-based buffer at 37 °C to denature content. Samples (10 to 20 μg) were resolved on SDS polyacrylamide gels and transferred to polyvinylidene difluoride membranes for blotting. After blocking with 5% dry nonfat milk (LabScientific #M0841) in PBS containing 0.1% Tween 20 (PBST), primary and secondary antibodies were sequentially applied along with PBST washing steps to detect proteins of interest as indicated in the text. The following primary antibodies were utilized: anti-Flag (Proteintech #66008-4-Ig), anti-Flag (D6W5B) (Cell Signaling Technology #14793S), anti-Flag (Bethyl Labs # A190-102A), anti-GAPDH (6C5) (MilliporeSigma #MAB374), anti-GFP (13.1 & 7.1) (Roche #11814460001), anti-GFP (Invitrogen #A6455), anti-HA (2-2.2.14) (Invitrogen #26183), anti-beta actin (8H10D10) (Cell Signaling Technology #3700), anti-KCTD1 (Abcepta #AP4955b), anti-KCTD15 (Proteintech #20128-1-AP), anti-AC1 (Proteintech # 55067-1-AP), anti-AC3 (Proteintech # 19492-1-AP), anti-AC5 (19D5.C1) (MilliporeSigma #MABS2049), and anti-AC9 (Bethyl Labs #A304-465A-T). The following HRP-conjugated secondary antibodies were used: anti-rabbit (Jackson ImmunoResearch #211-032-171) and anti-mouse (Jackson ImmunoResearch #115-035-174). Protein bands were visualized by exposing membranes to an ECL reagent followed by digital exposure utilizing the KwikQuant Imager (Kindle Biosciences #D1001). Band intensity was quantified using standard ImageJ tools.

IP. For western blotting, 75 μg of total lysate was rotated for 1 h at 4 °C in 500 μL lysis buffer containing anti-HA antibody (Invitrogen #26183; 500 ng) and Dynabeads Protein G (Invitrogen #10003D). Beads were then washed three times by rotation at 4 °C in 500 μL lysis buffer for 10 min. Beads were then resuspended in 50 μL SDS-based buffer and incubated for 15 min at 37 °C, and 20 μL of the sample was utilized for western blotting analysis as described above. For luminescence assays, 400 μg of total lysate was rotated for 2 h at 4 °C in 500 μL lysis buffer containing 10 μL anti-Flag magnetic agarose (Thermo Scientific Pierce #A36797). Agarose was washed three times by rotation at 4 °C in 500 μL lysis buffer for 10 min, and samples were resuspended in 70 μL lysis buffer for use directly in luminescence assays.

Dual luminescence assay. After overnight treatment with (R)-MG132 (Cayman Chemical #13697) at a final concentration of 10 μM, cells were lysed as described above in an ice-cold PBS supplemented with 0.5% n-Dodecanoylsucrose (EMD Millipore #324374-5GM), 150 mM NaCl, 1 M MgCl2, and protease inhibitor (Thermo Fisher Scientific #A32955). Measurements were made in 96-well opaque white-wall plates on a SPECTROstar Omega plate reader (BMG Labtech). Each sample was plated in two wells to separately record Fluc and Nano-luciferase (Nluc). Luminescence from Fluc was recorded after addition of 25 μL 2× Firefly substrate: 10 mM dithiothreitol, 1 mM adenosine triphosphate, and 3 mg/mL D-luciferin (Gold Biotechnology #LUCK-100) in lysis buffer. Luminescence from Nluc was recorded after addition of 25 μL 2× Nano-Glo substrate (Promega #N113A) in lysis buffer. IP ratio is reported as raw Fluc value divided by Nluc value.

Confocal imaging. HEK293 cells were grown on glass coverslips for transfection with AC5-Venus-P2A-mRuby3 and KCTD-myc-Flag plasmids at a 2:1 ratio. After 24 h, the growth media was replaced with OptiPRO SFM (Gibco #12309019), cells were maintained an additional 24 h, fixed with 4% PFA, and then mounted on slides. Cells were imaged through a 20× objective on a Leica Stellaris confocal microscope. Venus was excited by an OPSL 488 nm laser line and emission recorded through a HyD photomultiplier tube (PMT) set to collect a range from 517 to 558 nm. mRuby3 was excited by a DPSS 561 nm laser line with emission recorded through a HyD PMT from 566 to 712 nm. All imaging was performed with identical settings including laser intensity, digital gain, pinhole size, and line averaging. Individual fluorophore intensity was quantified for single cells using standard ImageJ tools.

Primary neuron culture. Whole striata were dissected from homozygous *CAMPER* pups at P0 and placed in ice-cold Hanks' Balanced Salt Solution (HBSS) containing Fetalgro (20%), NaHCO3 (4.2 mM), and 4-(2-hydroxyethyl)-1-piperazineetha nesulfonic acid (HEPES) (1 mM). Similar to previously described (47), striata were then washed in the same HBSS without Fetalgro followed by a 15-min digestion at 37 °C in a pH 7.2 buffer containing (in mM): NaCl (137), KCl (5), Na2HPO4 (7), HEPES (25), and 0.3 mg/mL papain (Worthington). Postdigestion, the striata were sequentially washed with HBSS + 20% FetalGro, HBSS, and neuronal growth media (Neurobasal-A solution containing 2 mM GlutaMAX, 2% B27 supplement, 100 units/mL penicillin, and 100 μg/mL streptomycin). Tissue was then mechanically triturated in growth media containing DNase I (0.05 U/μL) with a P1000

pipette. Dissociated neurons were then plated on poly-D-lysine (MilliporeSigma #P6407) coated German glass coverslips at 37 °C in a humidified incubator with constant 5% CO_2. After 2 d in culture, half of the neuron growth media was replaced with fresh growth media containing AAV particles as indicated in the text. Half media changes with regular neuronal growth media were then performed every 3 d.

Stereotaxic injection. As previously described (88), neonatal pups (P0–P2) were placed under ice anesthesia for 5 min and then arranged in a custom three-dimensional-printed device (89) on a rodent stereotaxic frame (Kopf Instruments) while maintaining thermal anesthesia. AAV particles were delivered through a Hamilton syringe coupled to a 30-gauge needle that was positioned by a manipulator into the dorsal striatum (AP: +2.4 mm anterior to lambda, ML ± 1.0 mm, DV −1.7 mm). Mice were bilaterally infused with 200 nL of AAV particles over a 4-min period. The needle then remained in place for an additional minute before slow removal from the brain. Pups were placed in a 33 °C incubator after the procedure whereupon recovery took place within 15 min. Pups were then returned to their home cage.

Acute brain slice preparation. As similarly described (47, 66), adult mice at 6 to 10 wk of age were isoflurane-anesthetized for decapitation, rapid brain extraction, and agarose mounted on a vibratome (Precisionary VF-310-0Z) in ice-cold oxygenated buffer consisting of (in mM): KCl (2.5), NMDG (93), glucose (25), HEPES (20), sodium ascorbate (5), sodium pyruvate (3), thiourea (2), NaH2PO4 (1.2), CaCl2 (0.5), MgCl2 (10), and NaHCO3 (30). Coronal sections were then cut at 300 μm thickness and incubated for 1 h at 34 °C in an oxygenated recovery buffer consisting of (in mM): NaCl (126), KCl (2.5), CaCl2 (2), MgCl2 (2), NaHCO3 (18), NaH2PO4 (1.2), and glucose (10). Slices were then maintained in oxygenated recording buffer for imaging experiments (described below).

FRET imaging of cells. Imaging of cAMP with the $^{T}Epac^{VV}$ FRET-based biosensor in HEK293 cells and *CAMPER* striatal neuron cultures was performed as previously described (29, 47). Cells were triple transfected with $^{T}Epac^{VV}$, Flag-AC5, and either pcDNA3.1 or KCTD1-myc-flag. Live cells on glass coverslips were transferred to a recording chamber and continuously perfused at a rate of approximately 2.5 mL/min with a buffer containing (in mM): NaCl (125), KCl (2.5), CaCl2 (2), MgCl2 (2), NaH2PO4 (1.25), NaHCO3 (10), glucose (10), and HEPES (5). Images were then collected through a 20× objective on a custom Olympus microscope where FRET donor excitation was achieved by white light illumination (CoolLED pE-400) filtered to 436 nm (Chroma ET436/20×). FRET donor (455 to 500 nm) and acceptor (500 to 600 nm) images were then simultaneously acquired by split emission (Cairn OptoSplit II; Chroma ET480/40 m and T455lp) through a Hamamatsu sCMOS (ORCA-Flash 4.0) at 10-s intervals. ImageJ tools were utilized to calculate FRET values from single-cell intensity, as described (47, 55). Forskolin (Cayman Chemical #11018) was bath applied as indicated in the text.

2-Photon FRET imaging in acute brain slices. As similarly described (47, 66), *CAMPER* brain slices were transferred to a recording chamber (Warner Instruments) for perfusion at approximately 2 mL/min with an ambient temperature oxygenated buffer consisting of (in mM): NaCl (125), KCl (2.5), CaCl2 (2), MgCl2 (2), NaH2PO4 (1.25), NaHCO3 (25), and glucose (25). FRET donor excitation was achieved by a Ti:Sapphire laser (Coherent Chameleon Vision S) tuned to 850 nm paired with simultaneous collection of donor (455 to 500 nm) and acceptor (526 to 571 nm) wavelengths through dual PMTs on a Zeiss 780 multiphoton confocal microscope through a 20× W Plan-Apochromat objective. XYZ image stacks were captured at 15-s intervals for experiments with bath application of forskolin, SKF38393, and quinpirole. For electrical stimulation experiments, a single Z plane was captured at either 0.5- or 1.0-s intervals and slices were stimulated (10 ms pulse; 650 μA) with a tungsten microelectrode (World Precision Instruments) inserted adjacent to the field of view controlled by Pulser (Prizmatix) software and a DS3 isolated current stimulator (Digitimer). FRET values were calculated from the intensity of the neuron cell body utilizing ImageJ tools. As indicated in the text, responses to dopamine were used to classify the MSN subtype based on directionality of the cAMP response (D1-MSN increased cAMP, whereas D2-MSN decreased cAMP). Forskolin (Cayman Chemical #11018), SKF38393 (Tocris #0922), quinpirole (Tocris #1061), SCH23390 (Cayman Chemical #15631), and sulpiride (TCI America #I08215G) were used as indicated in the text.

cAMP ELISA. Oxygenated *CAMPER* (AAV-hSyn-Cre-P2A-dTomato coinjected with AAV-FLEX-SaCas9-U6-Ctrl-sgRNA or AAV-FLEX-SaCas9-U6-Kctd1-sgRNA) brain slices were cut at 300 μm as described above and fluorescence was verified via 2-photon microscopy. Dorsal striatal tissue punches (2 mm) were then frozen, thawed, and homogenized in 0.1 M HCl. Total cAMP levels were determined utilizing a commercially available ELISA kit (ENZO Life Sciences #ADI-900-066) following the manufacturer's instructions as similarly reported (55, 65).

Backward walking. As previously described (55, 78), mice were positioned on our Rotarod in the reverse orientation with a barrier fitted to prevent turning. Mice were acclimated for 5 min before starting the rotarod acceleration rate at 4 rpm, thus ensuring that mice had to walk backward. Mice were tested on three intraday trials, with 5 min of rest between trials, and latency to fall was recorded.

Hindlimb clasping. As previously described (54), mice were tail suspended for 30 s while observing hindlimb motion patterns for scoring. Clasping was defined as retraction of hindlimb toward the body. A score of zero was assigned in the event of no clasping of either limb. Score of one for clasping of one limb for any period of time. Score of two for clasping one hindlimb for more than half the time. Score of three for clasping both hindlimbs for any period of time. Score of four for clasping both hindlimbs for more than half the time. Animals were scored three times and the average of the scores are presented in the results.

Accelerating rotarod. Following a standard protocol (56), motor learning was examined on a rotating rod (4-inch diameter) that accelerated from 4 to 60 rpm over 5 min. Mice were tested on three intraday trials, with a 5-min rest period between trials, over five consecutive days. Mice were then retested 7 and 14 d afterward. During each trial, the latency for the mouse to fall was recorded. If the mouse clung to the rod for a complete revolution, their trial ended early at that recorded time. The learning rate was calculated by subtracting the average latency on day 1 from day 5 and dividing by the number of days (5) (90).

Quantification and Statistical Analysis. Statistical analysis was performed using GraphPad Prism 10. Data are presented as the mean ± SE of the mean unless otherwise indicated in the text. The number of biological replicates, statistical tests performed, and *P* values are provided for each experiment in the appropriate figure legend. Sample size and biological replicate in Fig. 1*C* and *SI Appendix*, Fig. S1*A* presented as previously described "Superplot" style (91).

Data, Materials, and Software Availability. All study data are included in the article and/or *SI Appendix*.

ACKNOWLEDGMENTS. We are thankful to Dr. Kirill A. Martemyanov for kindly providing the CAMPER mice to our laboratory. This work was supported by institutional funds from Augusta University (Medical College of Georgia, Department of Pharmacology and Toxicology) and funding from the National Institute of Neurological Disorders and Stroke (1R01NS129554 to B.S.M.).

1. A. M. Graybiel, T. Aosaki, A. W. Flaherty, M. Kimura, The basal ganglia and adaptive motor control. *Science* **265**, 1826–1831 (1994).
2. B. Picconi *et al.*, Pathological synaptic plasticity in the striatum: Implications for Parkinson's disease. *Neurotoxicology* **26**, 779–783 (2005).
3. T. Wichmann, J. O. Dostrovsky, Pathological basal ganglia activity in movement disorders. *Neuroscience* **198**, 232–244 (2011).
4. J. M. Brotchie, Adjuncts to dopamine replacement: A pragmatic approach to reducing the problem of dyskinesia in Parkinson's disease. *Mov. Disord.* **13**, 871–876 (1998).
5. J. Jankovic, Dopamine depleters in the treatment of hyperkinetic movement disorders. *Expert. Opin. Pharmacother.* **17**, 2461–2470 (2016).
6. W. Shen, M. Flajolet, P. Greengard, D. J. Surmeier, Dichotomous dopaminergic control of striatal synaptic plasticity. *Science* **321**, 848–851 (2008).
7. C. R. Gerfen, D. J. Surmeier, Modulation of striatal projection systems by dopamine. *Annu. Rev. Neurosci.* **34**, 441–466 (2011).
8. S. M. Nicola, R. C. Malenka, Modulation of synaptic transmission by dopamine and norepinephrine in ventral but not dorsal striatum. *J. Neurophysiol.* **79**, 1768–1776 (1998).
9. N. X. Tritsch, B. L. Sabatini, Dopaminergic modulation of synaptic transmission in cortex and striatum. *Neuron* **76**, 33–50 (2012).
10. P. M. Knappskog, T. Flatmark, J. Mallet, B. Ludecke, K. Bartholome, Recessively inherited L-DOPA-responsive dystonia caused by a point mutation (Q381K) in the tyrosine hydroxylase gene. *Hum. Mol. Genet.* **4**, 1209–1212 (1995).
11. B. Ludecke, B. Dworniczak, K. Bartholome, A point mutation in the tyrosine hydroxylase gene associated with Segawa's syndrome. *Hum. Genet.* **95**, 123–125 (1995).
12. M. A. Kurian *et al.*, Homozygous loss-of-function mutations in the gene encoding the dopamine transporter are associated with infantile parkinsonism-dystonia. *J. Clin. Invest.* **119**, 1595–1603 (2009).
13. C. Klein *et al.*, Epsilon-sarcoglycan mutations found in combination with other dystonia gene mutations. *Ann. Neurol.* **52**, 675–679 (2002).

14. K. Nakamura *et al.*, De Novo mutations in GNAO1, encoding a Galphao subunit of heterotrimeric G proteins, cause epileptic encephalopathy. *Am. J. Hum. Genet.* **93**, 496–505 (2013).
15. T. Fuchs *et al.*, Mutations in GNAL cause primary torsion dystonia. *Nat. Genet.* **45**, 88–92 (2013).
16. K. Lohmann *et al.*, Novel GNB1 mutations disrupt assembly and function of G protein heterotrimers and cause global developmental delay in humans. *Hum. Mol. Genet.* **26**, 1078–1086 (2017).
17. C. P. Diggle *et al.*, Biallelic mutations in PDE10A Lead to Loss of striatal PDE10A and a hyperkinetic movement disorder with onset in infancy. *Am. J. Hum. Genet.* **98**, 735–743 (2016).
18. N. E. Mencacci *et al.*, De Novo mutations in PDE10A cause childhood-onset chorea with bilateral striatal lesions. *Am. J. Hum. Genet.* **98**, 763–771 (2016).
19. K. W. Lee *et al.*, Impaired D2 dopamine receptor function in mice lacking type 5 adenylyl cyclase. *J. Neurosci.* **22**, 7931–7940 (2002).
20. M. Fernandez *et al.*, Familial dyskinesia and facial myokymia (FDFM): A novel movement disorder. *Ann. Neurol.* **49**, 486–492 (2001).
21. R. Sadana, C. W. Dessauer, Physiological roles for G protein-regulated adenylyl cyclase isoforms: Insights from knockout and overexpression studies. *Neurosignals* **17**, 5–22 (2009).
22. R. K. Sunahara, C. W. Dessauer, A. G. Gilman, Complexity and diversity of mammalian adenylyl cyclases. *Annu. Rev. Pharmacol. Toxicol.* **36**, 461–480 (1996).
23. J. J. Tesmer, R. K. Sunahara, A. G. Gilman, S. R. Sprang, Crystal structure of the catalytic domains of adenylyl cyclase in a complex with Gsalpha.GTPgammaS. *Science* **278**, 1907–1916 (1997).
24. J. J. Tesmer *et al.*, Two-metal-Ion catalysis in adenylyl cyclase. *Science* **285**, 756–760 (1999).
25. Y. C. Yen *et al.*, Structure of adenylyl cyclase 5 in complex with Gbetagamma offers insights into ADCY5-related dyskinesia. *Nat. Struct. Mol. Biol.* **31**, 1189–1197 (2024).
26. W. Hu *et al.*, The complex of TRIP-Br 1 and XIAP ubiquitinates and degrades multiple adenylyl cyclase isoforms. *Elife* **6**, e28021 (2017).
27. K. Xie *et al.*, Stable G protein–effector complexes in striatal neurons: Mechanism of assembly and role in neurotransmitter signaling. *Elife* **4**, e10451 (2015).
28. M. Brockmann *et al.*, Genetic wiring maps of single-cell protein states reveal an off-switch for GPCR signalling. *Nature* **546**, 307–311 (2017).
29. D. C. Sloan, C. E. Cryan, B. S. Muntean, Multiple potassium channel tetramerization domain (KCTD) family members interact with Gbetagamma, with effects on cAMP signaling. *J. Biol. Chem.* **299**, 102924 (2023).
30. B. D. Young, J. Sha, A. A. Vashisht, J. A. Wohlschlegel, Human multisubunit E3 ubiquitin ligase required for heterotrimeric G-Protein beta-Subunit Ubiquitination and downstream signaling. *J. Proteome Res.* **20**, 4318–4330 (2021).
31. R. Turecek *et al.*, Auxiliary GABAB receptor subunits uncouple G protein betagamma subunits from effector channels to induce desensitization. *Neuron* **82**, 1032–1044 (2014).
32. R. Azizieh *et al.*, Progressive myoclonic epilepsy-associated gene KCTD7 is a regulator of potassium conductance in neurons. *Mol. Neurobiol.* **44**, 111–121 (2011).
33. E. De Smaele *et al.*, Identification and characterization of KCASH2 and KCASH3, 2 novel Cullin3 adaptors suppressing histone deacetylase and Hedgehog activity in medulloblastoma. *Neoplasia* **13**, 374–385 (2011).
34. K. Kasahara *et al.*, Ubiquitin-proteasome system controls ciliogenesis at the initial step of axoneme extension. *Nat. Commun.* **5**, 5081 (2014).
35. G. Smaldone *et al.*, Cullin 3 Recognition is not a universal property among KCTD proteins. *PLoS One* **10**, e0126808 (2015).
36. Y. Bayón *et al.*, KCTD5, a putative substrate adaptor for cullin3 ubiquitin ligases. *FEBS. J* **275**, 3900–3910 (2008).
37. H. C. Yen, Q. Xu, D. M. Chou, Z. Zhao, S. J. Elledge, Global protein stability profiling in mammalian cells. *Science* **322**, 918–923 (2008).
38. Y. Liao, D. C. Sloan, J. H. Widjaja, B. S. Muntean, KCTD5 Forms hetero-oligomeric complexes with various members of the KCTD protein family. *Int. J. Mol. Sci.* **24**, 14317 (2023).
39. O. Gokce *et al.*, Cellular taxonomy of the mouse striatum as revealed by single-cell RNA-seq. *Cell Rep.* **16**, 1126–1137 (2016).
40. K. S. Kim *et al.*, Adenylyl cyclase type 5 (AC5) is an essential mediator of morphine action. *Proc. Natl. Acad. Sci. U.S.A.* **103**, 3908–3913 (2006).
41. G. C. Wu, H. L. Lai, Y. W. Lin, Y. T. Chu, Y. Chern, N-glycosylation and residues Asn805 and Asn890 are involved in the functional properties of type VI adenylyl cyclase. *J. Biol. Chem.* **276**, 35450–35457 (2001).
42. A. Helenius, M. Aebi, Roles of N-linked glycans in the endoplasmic reticulum. *Annu. Rev. Biochem.* **73**, 1019–1049 (2004).
43. T. Suzuki, A. Seko, K. Kitajima, Y. Inoue, S. Inoue, Identification of peptide:N-glycanase activity in mammalian-derived cultured cells. *Biochem. Biophys. Res. Commun.* **194**, 1124–1130 (1993).
44. T. Suzuki, C. Huang, H. Fujihira, The cytoplasmic peptide:N-glycanase (NGLY1)–Structure, expression and cellular functions. *Gene* **577**, 1–7 (2016).
45. J. H. Stack, M. Whitney, S. M. Rodems, B. A. Pollok, A ubiquitin-based tagging system for controlled modulation of protein stability. *Nat. Biotechnol.* **18**, 1298–1302 (2000).
46. J. B. Klarenbeek, J. Goedhart, M. A. Hink, T. W. Gadella, K. Jalink, A mTurquoise-based cAMP sensor for both FLIM and ratiometric read-out has improved dynamic range. *PLoS One* **6**, e19170 (2011).
47. B. S. Muntean *et al.*, Interrogating the spatiotemporal landscape of neuromodulatory GPCR signaling by real-time imaging of cAMP in intact neurons and circuits. *Cell Rep.* **22**, 255–268 (2018).
48. A. C. Hunker *et al.*, Conditional single vector CRISPR/SaCas9 viruses for efficient mutagenesis in the adult mouse nervous system. *Cell Rep.* **30**, 4303–4316.e6 (2020).
49. M. Negrini, G. Wang, A. Heuer, T. Bjorklund, M. Davidsson, AAV production everywhere: A simple, fast, and reliable protocol for In-house AAV vector production based on chloroform extraction. *Curr. Protoc. Neurosci.* **93**, e103 (2020).
50. I. Matsuoka, Y. Suzuki, N. Defer, H. Nakanishi, J. Hanoune, Differential expression of type I, II, and V adenylyl cyclase gene in the postnatal developing rat brain. *J. Neurochem.* **68**, 498–506 (1997).
51. R. L. Albin, A. B. Young, J. B. Penney, The functional anatomy of basal ganglia disorders. *Trends Neurosci.* **12**, 366–375 (1989).
52. A. G. Nair, O. Gutierrez-Arenas, O. Eriksson, P. Vincent, J. Hellgren Kotaleski, Sensing positive versus negative reward signals through adenylyl cyclase-coupled GPCRs in direct and indirect pathway striatal medium spiny neurons. *J. Neurosci.* **35**, 14017–14030 (2015).
53. G. Cui *et al.*, Concurrent activation of striatal direct and indirect pathways during action initiation. *Nature* **494**, 238–242 (2013).
54. S. J. Guyenet *et al.*, A simple composite phenotype scoring system for evaluating mouse models of cerebellar ataxia. *J. Vis. Exp.* **39**, 1–3 (2010).
55. B. S. Muntean *et al.*, Galphao is a major determinant of cAMP signaling in the pathophysiology of movement disorders. *Cell Rep.* **34**, 108718 (2021).
56. J. H. Widjaja, D. C. Sloan, J. A. Hauger, B. S. Muntean, Customizable open-source rotating rod (Rotarod) enables robust low-cost assessment of motor performance in mice. *eNeuro* **10,** 1–16 (2023).
57. C. Qi, S. Sorrentino, O. Medalia, V. M. Korkhov, The structure of a membrane adenylyl cyclase bound to an activated stimulatory G protein. *Science* **364**, 389–394 (2019).
58. B. Khanppnavar *et al.*, Regulatory sites of CaM-sensitive adenylyl cyclase AC8 revealed by cryo-EM and structural proteomics. *EMBO Rep.* **25**, 1513–1540 (2024).
59. Z. Ding *et al.*, Genome-wide small interfering RNA screening reveals a role for Cullin3–Really interesting new gene ligase signaling in heterologous sensitization of Adenylyl Cyclase. *J. Pharmacol. Exp. Ther.* **372**, 267–276 (2020).
60. Z. Ding, G. T. Knipp, R. M. van Rijn, J. A. Chester, V. J. Watts, The CUL3/neddylation inhibitor MLN4924 reduces ethanol-induced locomotor sensitization and inflammatory pain allodynia in mice. *Behav. Brain Res.* **399**, 113051 (2021).
61. T. B. Doyle *et al.*, Identification of novel Adenylyl Cyclase 5 (AC5) signaling networks in D(1) and D(2) Medium spiny neurons using bimolecular fluorescence complementation screening. *Cells* **8**, 1468 (2019).
62. S. Ferre *et al.*, G protein-coupled receptor-effector macromolecular membrane assemblies (GEMMAs). *Pharmacol. Ther.* **231**, 107977 (2022).
63. S. Esmail, M. F. Manolson, Advances in understanding N-glycosylation structure, function, and regulation in health and disease. *Eur. J. Cell Biol.* **100**, 151186 (2021).
64. X. Teng *et al.*, KCTD: A new gene family involved in neurodevelopmental and neuropsychiatric disorders. *CNS Neurosci. Ther.* **25**, 887–902 (2019).
65. L. P. Sutton *et al.*, NF1-cAMP signaling dissociates cell type-specific contributions of striatal medium spiny neurons to reward valuation and motor control. *PLoS Biol.* **17**, e3000477 (2019).
66. B. S. Muntean, M. T. Dao, K. A. Martemyanov, Allostatic changes in the cAMP System drive opioid-induced adaptation in striatal dopamine signaling. *Cell Rep.* **29**, 946–960.e2 (2019).
67. S. N. Schiffmann, O. Jacobs, J. J. Vanderhaeghen, Striatal restricted adenosine A2 receptor (RDC8) is expressed by enkephalin but not by substance P neurons: An in situ hybridization histochemistry study. *J. Neurochem.* **57**, 1062–1067 (1991).
68. H. W. Nam, R. C. Bruner, D. S. Choi, Adenosine signaling in striatal circuits and alcohol use disorders. *Mol. Cells* **36**, 195–202 (2013).
69. S. Tanaka, K. Ishii, K. Kasai, S. O. Yoon, Y. Saeki, Neural expression of G protein-coupled receptors GPR3, GPR6, and GPR12 up-regulates cyclic AMP levels and promotes neurite outgrowth. *J. Biol. Chem.* **282**, 10506–10515 (2007).
70. M. K. Lobo, Y. Cui, S. B. Ostlund, B. W. Balleine, X. W. Yang, Genetic control of instrumental conditioning by striatopallidal neuron-specific S1P receptor Gpr6. *Nat. Neurosci.* **10**, 1395–1397 (2007).
71. T. Iwamoto *et al.*, Motor dysfunction in type 5 adenylyl cyclase-null mice. *J. Biol. Chem.* **278**, 16936–16940 (2003).
72. M. A. Kheirbek *et al.*, Adenylyl cyclase type 5 contributes to corticostriatal plasticity and striatum-dependent learning. *J. Neurosci.* **29**, 12115–12124 (2009).
73. B. Liang *et al.*, Striatal direct pathway neurons play leading roles in accelerating rotarod motor skill learning. *iScience* **25**, 104245 (2022).
74. J. Jankovic, Medical treatment of dystonia. *Mov. Disord.* **28**, 1001–1012 (2013).
75. I. Masuho *et al.*, A Global map of G protein signaling regulation by RGS proteins. *Cell* **183**, 503–521.e19 (2020).
76. J. Gibon *et al.*, The X-linked inhibitor of apoptosis regulates long-term depression and learning rate. *FASEB J.* **30**, 3083–3090 (2016).
77. N. E. Mencacci *et al.*, A missense mutation in KCTD17 causes autosomal dominant myoclonus-dystonia. *Am. J. Hum. Genet.* **96**, 938–947 (2015).
78. B. S. Muntean *et al.*, Members of the KCTD family are major regulators of cAMP signaling. *Proc. Natl. Acad. Sci. U.S.A.* **119**, e2119237119 (2022).
79. C. Ruangchan *et al.*, Genetic variants in KCTD1 are associated with isolated dental anomalies. *Int. J. Mol. Sci.* **25**, 5179 (2024).
80. A. G. Marneros *et al.*, Mutations in KCTD1 cause scalp-ear-nipple syndrome. *Am. J. Hum. Genet.* **92**, 621–626 (2013).
81. G. Smaldone *et al.*, Molecular basis of the scalp-ear-nipple syndrome unraveled by the characterization of disease-causing KCTD1 mutants. *Sci. Rep.* **9**, 10519 (2019).
82. N. Balasco *et al.*, Structural studies of KCTD1 and its disease-causing mutant P20S provide insights into the protein function and misfunction. *Int. J. Biol. Macromol.* **277**, 134390 (2024).
83. X. Miao, J. Wu, H. Chen, G. Lu, Comprehensive analysis of the structure and function of peptide: N-Glycanase 1 and relationship with congenital disorder of deglycosylation. *Nutrients* **14**, 1690 (2022).
84. C. Lam *et al.*, Prospective phenotyping of NGLY1-CDDG, the first congenital disorder of deglycosylation. *Genet. Med.* **19**, 160–168 (2017).
85. H. Fujihira *et al.*, Lethality of mice bearing a knockout of the Ngly1-gene is partially rescued by the additional deletion of the Engase gene. *PLoS Genet.* **13**, e1006696 (2017).
86. X. Gao, R. Sadana, C. W. Dessauer, T. B. Patel, Conditional stimulation of type V and VI adenylyl cyclases by G protein betagamma subunits. *J. Biol. Chem.* **282**, 294–302 (2007).
87. J. P. Concordet, M. Haeussler, CRISPOR: Intuitive guide selection for CRISPR/Cas9 genome editing experiments and screens. *Nucleic Acids Res.* **46**, W242–W245 (2018).
88. S. Y. Chen, H. Y. Kuo, F. C. Liu, Stereotaxic surgery for genetic manipulation in striatal cells of neonatal mouse brains. *J. Vis. Exp.* **137**, 1–6 (2018)10.3791/57270.
89. P. R. Olivetti, C. O. Lacefield, C. Kellendonk, A device for stereotaxic viral delivery into the brains of neonatal mice. *Biotechniques* **69**, 307–312 (2020).
90. C. A. French *et al.*, An aetiological Foxp2 mutation causes aberrant striatal activity and alters plasticity during skill learning. *Mol. Psychiatry* **17**, 1077–1085 (2012).
91. S. J. Lord, K. B. Velle, R. D. Mullins, L. K. Fritz-Laylin, SuperPlots: Communicating reproducibility and variability in cell biology. *J. Cell Biol.* **219**, e202001064(2020).